RESEARCH ARTICLE | SEPTEMBER 23 2025

Quantum dynamics at conical intersections in solution. II. Multiconfigurational wavefunction dynamics at finite temperature

Bartosz Błasiak ; Dominik Brey ; Rocco Martinazzo ; Irene Burghardt

J. Chem. Phys. 163, 124109 (2025)
https://doi.org/10.1063/5.0284504

The Journal of Chemical Physics ARTICLE pubs.aip.org/aip/jcp

Quantum dynamics at conical intersections in solution. II. Multiconfigurational wavefunction dynamics at finite temperature

Cite as: J. Chem. Phys. 163, 124109 (2025); doi: 10.1063/5.0284504
Submitted: 8 June 2025 • Accepted: 25 August 2025 •
Published Online: 23 September 2025

Bartosz Błasiak,[1] Dominik Brey,[1] Rocco Martinazzo,[2] and Irene Burghardt[1,a)]

AFFILIATIONS

[1] Institute of Physical and Theoretical Chemistry, Goethe University Frankfurt, Max-von-Laue-Str. 7, 60438 Frankfurt, Germany
[2] Department of Chemistry, Università degli Studi di Milano, Via Golgi 19, 20133 Milano, Italy

[a)] **Author to whom correspondence should be addressed:** burghardt@chemie.uni-frankfurt.de

ABSTRACT

The multiplicative neural network (m-NN) potentials described in Paper I [Błasiak *et al.*, J. Chem. Phys. **163**, 124108 (2025)] are employed to carry out multi-layer multi-configuration time-dependent Hartree simulations of the dynamics at a conical intersection including environmental effects. For a model of *cis–trans* isomerization in a protonated Schiff base, vibronic effects induced by intramolecular torsional and bond-length-alternation modes act concertedly with a collective environmental mode, which plays the role of an effective tuning mode. The latter is coupled to a residual environment, and the combination of the effective and residual modes conforms to an overdamped Brownian oscillator type spectral density. Thermal averages are included by the thermofield dynamics approach, in line with the thermal Hamiltonian developed in Paper I. The m-NN potentials, modeled according to the regularized diabatic states representation, permit an accurate representation of the vibronic coupling Hamiltonian beyond a linear vibronic coupling model. The initial excited-state dynamics is determined by the approach to a curved conical intersection seam, followed by a strongly dissipative phase leading to equilibration in the adiabatic ground state. The characteristic inertial time scale of the environment impacts not only the time of approach to the conical intersection seam but also the isomerization yield. The present study makes first steps toward extending the m-NN approach to a treatment of collective environmental non-equilibrium evolution on par with intramolecular excited-state nonadiabatic dynamics.

I. INTRODUCTION

The dynamical description of excited-state dynamics in a chromophore in contact with an environment is challenging due to the large number of degrees of freedom that are involved and their specific effects on the electronically excited states. A paradigm situation is excited-state dynamics at a conical intersection (CI),[1,2] whose topology can be influenced in specific ways by the environment. Among the available methods, a quantum-mechanics/molecular mechanics (QM/MM) partitioning of the system into chromophore vs environment subspaces is frequently employed,[3–7] combined with approximate dynamical methods, typically of surface-hopping or mean-field Ehrenfest type.

Conversely, quantum dynamical techniques are often used in conjunction with model Hamiltonians,[1,2,8] both at the wavefunction level and at the density matrix level.[9,10] Advanced quantum–classical techniques, notably the quantum–classical Liouville equation (QCLE) have also been employed in this context.[11] The advent of highly efficient tensor network methods such as the multi-configuration time-dependent Hartree (MCTDH) method[12] and its multi-layer variant (ML-MCTDH),[13–16] along with the related matrix product states (MPS) method,[17,18] has made the treatment of system-bath dynamics feasible within a wavefunction setting, since hundreds of degrees of freedom can be accommodated within typical system–bath Hamiltonians. Meanwhile, applications in an *on-the-fly* context are currently limited to small systems.

In view of generating accurate excited-state potentials for quantum dynamical propagation in many dimensions, machine learning methods have led to new perspectives in recent years.[19–25] Our recent work on the multiplicative neural network (m-NN) approach[26,27] is one example in this direction, among many related efforts.

As detailed in the companion paper (denoted Paper I in the following),[28] the specific development that is of interest in the present study relates to including collective environmental coordinates into machine-learned vibronic Hamiltonian representations. While we will consider the most common example of an energy gap coordinate[29–31] that introduces tuning type effects at a conical intersection, the construction as such is more general and includes, e.g., collective coupling effects, as explained in Paper I.[28] Even though such coordinates have been previously employed in the context of linear vibronic coupling (LVC) models,[2,32–35] the combination with NN potentials opens the possibility to move toward more accurate potential representations. Furthermore, these developments will lead to new strategies where collective coordinates are sampled from atomistic simulations and subsequently combined with a quantum dynamical or quantum–classical treatment.

Here, we demonstrate for a model potential describing *cis–trans* isomerization of a protonated Schiff base (PSB) in solution[36,37] that the m-NN potentials of Paper I[28] are highly suitable for quantum propagation using the ML-MCTDH method, in excellent agreement with the dynamics obtained for the reference potentials. As detailed in Paper I,[28] the dominant effect of a polar/polarizable solvent environment can be subsumed in a spectral density (SD) representing collective reorientational motion,[29,38,39] which is induced by photoexcitation to an excited state whose charge distribution differs significantly from the initial state. As a result, excited-state lifetimes and product distributions can depend on the solvent, as has been observed experimentally.[40–44] For the model system described in Refs. 36 and 37, this effect has been previously described in preliminary quantum dynamical calculations[45] and surface-hopping calculations relying on an effective polarization coordinate.[46,47] In the present work, the solvent environment is represented by a spectral density in conjunction with the collective-mode construction developed in Refs. 32–35 and generalized to NN potentials in Paper I.[28]

As explained in Paper I, our dynamical study of the chromophore-environment system is based on a thermal Hamiltonian resulting from the thermofield dynamics (TFD) approach.[48–50] In the photochemical context under study, the solvent is initially equilibrated to the electronic ground state, and a non-equilibrium dynamics of the solvent coupled to the chromophore results from photoexcitation. In Paper I,[28] we described the resulting thermal Hamiltonian, which acts on a wavefunction in a duplicated Hilbert space, according to the TFD theory. In the present paper, the resulting dynamical propagation is carried out using the ML-MCTDH method.

The remainder of this manuscript is structured as follows: Sec. II addresses the relevant vibronic Hamiltonian including neural network potentials and thermofields; Sec. III describes the implementation using the ML-MCTDH method; Sec. IV summarizes several specific analysis methods; Sec. V presents the dynamical simulations; and Section VI concludes with a discussion.

II. VIBRONIC COUPLING HAMILTONIAN AND THERMOFIELDS

Here, we provide an overview of the vibronic coupling Hamiltonian (Sec. II A), along with the NN construction (Sec. II B) and the thermofield dynamics description (Sec. II C), leading to the thermal Hamiltonian that is employed in the quantum dynamical simulations.

A. Vibronic coupling Hamiltonian

Following up on Paper I,[28] a two-state Hamiltonian is formulated for a subset of intramolecular modes—here, a torsional mode (ϕ) and a bond-length-alternation mode (r) that play a key role in the isomerization dynamics—along with a set of reservoir modes. The latter are sampled from an overdamped Brownian oscillator spectral density[29,38,39,51] representing a solvent environment. Using orthogonal coordinate transformations, these reservoir modes are recast as a collective coordinate (Q) coupled to a residual environment ($\{Q'_n\}$).[28] In the present context, we add a second local reservoir in the low-frequency range ($\{Q''_n\}$), which acts on the torsional mode such as to induce frictional effects leading to relaxation following passage through the conical intersection. Hence, the overall Hamiltonian reads as follows:

$$\widehat{\boldsymbol{H}}(\widehat{\phi},\widehat{r},\widehat{Q},\{\widehat{Q}'_n\},\{\widehat{Q}''_n\}) = (\widehat{T}_S+\widehat{T}_{\rm eff})\mathbf{1} + \widehat{\boldsymbol{V}}_{\rm RDS}(\widehat{\phi},\widehat{r},\widehat{Q}) + \widehat{H}^{(Q)}_{\rm res}(\widehat{Q},\{\widehat{Q}'_n\})\mathbf{1} + \widehat{H}^{(\phi)}_{\rm res}(\widehat{\phi},\{\widehat{Q}''_n\})\mathbf{1}. \tag{1}$$

In Eq. (1), the subsystem (S) and effective-mode (eff) kinetic energies, comprising contributions from the vibronically active modes (ϕ, r, Q), are electronically diagonal,

$$\widehat{T}_S+\widehat{T}_{\rm eff} = \frac{1}{2}\omega_\phi\widehat{p}^2_\phi + \frac{1}{2}\omega_r\widehat{p}^2_r + \frac{1}{2}\Omega\,\widehat{P}^2, \tag{2}$$

where the momentum operators are given as $\widehat{p}_\phi = -i\partial/\partial\phi$ and analogously for the other coordinates, and mass- and frequency-weighted coordinates are used as in Paper I.[28] The frequencies $\omega_r = 1083$ cm^{-1} and $\omega_\phi = 590$ cm^{-1} correspond to harmonic approximants at the ground-state equilibrium geometry of the reference potential,[37] while Ω is the effective-mode frequency of the environment; here, $\Omega_s = 77$ cm^{-1} and $\Omega_f = 229$ cm^{-1} for two types of solvents ("slow" vs "fast") that are addressed in this study (see Sec. III for details). The local reservoirs (res) represented by $\widehat{H}^{(Q)}_{\rm res}$ and $\widehat{H}^{(\phi)}_{\rm res}$ are specified in the following. The vibronic coupling part of the Hamiltonian, $\widehat{\boldsymbol{V}}_{\rm RDS}$, represents a generalization of the regularized diabatic states (RDS)[52,53] model to periodic potentials, as detailed in Paper I.[28] This potential includes the collective environmental mode Q on par with the intramolecular modes (r,ϕ), see Eq. (14) of Paper I,[28]

$$\widehat{\boldsymbol{V}}_{\rm RDS}(\widehat{\phi},\widehat{r},\widehat{Q}) = \Sigma(\widehat{\phi},\widehat{r},\widehat{Q})\mathbf{1} + \frac{\Delta(\widehat{\phi},\widehat{r},\widehat{Q})}{\Delta^{(1)}(\widehat{\phi},\widehat{r},\widehat{Q})} \times \begin{pmatrix} \Delta_0(\widehat{r},\widehat{Q}) & \zeta(\widehat{r},\widehat{Q})\cos\widehat{\phi} \\ \zeta(\widehat{r},\widehat{Q})\cos\widehat{\phi} & -\Delta_0(\widehat{r},\widehat{Q}) \end{pmatrix}, \tag{3}$$

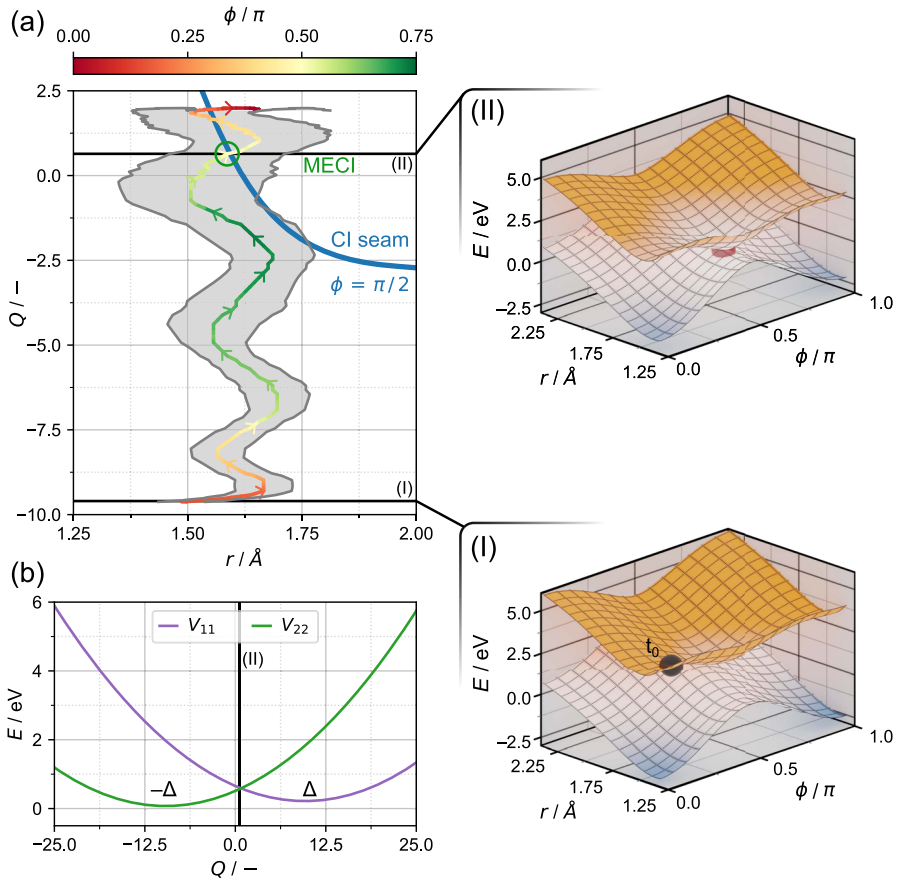

FIG. 1. Complementary to Fig. 1 of Paper I,[28] the topology of the symmetry-allowed conical intersection under study is shown. (a) Wavepacket motion toward the conical intersection seam and, specifically, the MECI. The wavepacket is projected onto the (r, Q) plane at $\phi = \pi/2$, and the displacement in the torsion is indicated by color coding. The initial condition (r.h.s. panel I) is at a distance from the CI seam, but it allows a barrierless path toward the MECI (r.h.s. panel II). The wavepacket path corresponds to the "slow" solvent dynamics shown in Figs. 5(g)–5(l), entailing a non-reactive evolution with the wavepacket returning to the *cis* ($\phi = 0$) ground state minimum. (b) The diabatic collective-mode potentials are shown for a PES section along the MECI. The initial condition for the solvent is $\langle Q \rangle = -\Delta$.

where the diabatic coupling is expanded around the high-symmetry reference geometry $\cos\phi_0 = 0$ and all quantities are defined in Paper I.[28]

Figure 1 illustrates the conical intersection topology described by this model, featuring a curved conical intersection seam, which is reached by concerted motion of the vibronically active coordinates (ϕ, r, Q). As illustrated in the figure, the minimum energy CI (MECI) point plays a critical role in directing the nonadiabatic dynamics. As can also be inferred from the wavepacket path shown in the figure, motion in the slow environmental coordinate (Q) is essential in order to reach the CI seam.

B. Neural network potentials

In the present approach, Eq. (3) is mapped onto a multiplicative NN potential (see Paper I[28]), $\widehat{V}^{\mathrm{RDS}}_{mn}(\widehat{\phi}, \widehat{r}, \widehat{Q}) \approx \widehat{V}^{\mathrm{NN}}_{mn}(\widehat{\phi}, \widehat{r}, \widehat{Q})$, with

$$\widehat{V}_{\mathrm{NN}}(\widehat{\phi}, \widehat{r}, \widehat{Q}) = \sum_{m,n=1}^{2} \left(\mu^{(2)}_{mn} + \sum_{i=1}^{N_{\mathrm{NN}}} \omega^{(2)}_{i,mn} \widehat{F}_{mn,i\phi}(\cos\widehat{\phi}) \widehat{F}_{mn,ir}(\widehat{r}) \widehat{F}_{mn,iQ}(\widehat{Q}) \right) |m\rangle\langle n|, \tag{4}$$

where $\omega^{(2)}_{i,mn}$ and $\mu^{(2)}_{mn}$ are outer-layer weights and biases, respectively, whereas $\omega^{(1)}_{id,mn}$ and $\mu^{(1)}_{id,mn}$ are inner (hidden)-layer weights and biases, respectively.[26,27] Furthermore, N_{NN} denotes the number of NN nodes. In contrast to Eq. (3), the m-NN form of Eq. (4) is tailored to the sum-of-products (SOP) form of the multiconfigurational wavefunction to be discussed in Sec. III.

As detailed in Paper I,[28] the advantage of using the collective environmental coordinate Q is the low dimensionality of the neural network fit, which is restricted to the vibronically active modes (ϕ, r, Q), where Q subsumes the vibronic tuning effects exerted by the multi-dimensional environment. In the present NN protocol (see Paper I[28]), the input data were already given in terms of the collective mode Q, but a more general NN scheme would involve

extracting the cumulative coordinate(s), e.g., from atomistic simulations. Such an NN protocol would also include the fluctuation dynamics of Q, induced by the residual modes $\{Q'\}$. In contrast, in our present setup, fluctuations in the Q mode were not explicitly included in the NN fit. Instead, a thermal solvent distribution is added *a posteriori* in terms of a thermal Hamiltonian within the TFD approach, as explained in Subsection II C.

C. Thermofield dynamics

Following Paper I[28] (Sec. IV), we combine the Hamiltonian of Eq. (1) with the NN potentials of Eq. (4) and a TFD treatment of the solvent. A variant of the TFD approach is employed,[49,50,54] where an inverse Bogoliubov transformation (iBT) is carried out such as to shift the temperature dependence from the initial condition into the Hamiltonian [see Eqs. (32)–(34) of Paper I[28] and Ref. 55]. This variant, referred to as iBT approach in the following, conveniently permits using zero-temperature initial conditions. In this context, we include two features that are essential for our treatment: first, the thermalized reference state of the solvent is displaced in coordinate space, corresponding to a shifted ground state equilibrium geometry [see Fig. 1(b)], and second, the TFD approach is adapted to the hierarchical structure of the effective/residual environment. As a result, the following thermalized version of the Hamiltonian of Eq. (1), in conjunction with the NN potentials, is employed in the simulations:

$$\widehat{\boldsymbol{H}}_T^{\theta} = (\widehat{T}_S + \widehat{T}_{\rm eff})\mathbf{1} + \widehat{\boldsymbol{V}}_{\rm NN} + \Delta\widehat{\boldsymbol{H}}_{T,\rm eff}^{\theta} + \widehat{H}_{T,\rm res}^{(Q)}\mathbf{1} + \widehat{H}_{\rm res}^{(\phi)}\mathbf{1}, \tag{5}$$

where the superscript θ indicates the iBT Hamiltonian, associated with the parameter $\theta = \operatorname{arctanh}(\exp(-\omega/(2k_BT)))$. In this NN/TFD Hamiltonian, two temperature-dependent terms appear, related to the solvent subspace $(Q, \{Q'_n\})$, while the second local reservoir $(\{Q''_n\})$ is not thermalized. (In fact, as detailed in the following, a phenomenological Ohmic damping term at zero temperature is added to the torsional mode.) In Eq. (5), the first temperature-dependent term is a thermal correction term in the effective-mode (Q) subspace [see Eq. (48) of Paper I[28]],

$$\Delta\widehat{\boldsymbol{H}}_{T,\rm eff}^{\theta}(\widehat{Q},\widetilde{Q}) = \widehat{\boldsymbol{H}}_{T,\rm eff}^{\theta}(\widehat{Q},\widetilde{Q}) - \widehat{\boldsymbol{H}}_{\rm eff}(\widehat{Q}), \tag{6}$$

where $\widehat{\boldsymbol{H}}_{\rm eff}(\widehat{Q})$ is a linear vibronic coupling approximation to the Q dependence of the NN potential,

$$\widehat{\boldsymbol{H}}_{\rm eff}(\widehat{Q}) = \boldsymbol{\sigma}_z C\widehat{Q}_\Delta + \frac{\Omega}{2}(\widehat{Q}_\Delta^2 + \widehat{P}^2)\mathbf{1}, \tag{7}$$

where $\widehat{Q}_\Delta = \widehat{Q} - \Delta$ and $\Delta = \kappa/\Omega$ is the displaced equilibrium geometry of the reference state. Analogously, $\widehat{\boldsymbol{H}}_{T,\rm eff}^{\theta}(Q,\widetilde{Q})$ is the corresponding thermalized expression,

$$\widehat{\boldsymbol{H}}_{T,\rm eff}^{\theta}(\widehat{Q},\widetilde{Q}) = \boldsymbol{\sigma}_z(C\cosh(\theta)\widehat{Q}_{\Delta_\theta} + C\sinh(\theta)\widetilde{Q}_{\Delta_\theta}) + \frac{\Omega}{2}(\widehat{Q}_{\Delta_\theta}^2 + \widehat{P}^2 - \widetilde{Q}_{\Delta_\theta}^2 - \widetilde{P}^2)\mathbf{1}, \tag{8}$$

featuring a pair of real/tilde modes $(\widehat{Q},\widetilde{Q})$, where the shift is now temperature-dependent, i.e., $\widehat{Q}_{\Delta_\theta} \equiv \widehat{Q} - \Delta_\theta$, with $\Delta_\theta = \Delta(1 - e^{-\theta})$ (see Paper I[28]).

The second temperature-dependent term in Eq. (5) relates to the residual solvent space,

$$\widehat{H}_{T,\rm res}^{(Q)}(\widehat{Q},\widetilde{Q},\{\widehat{Q}'_n\},\{\widetilde{Q}'_n\}) = \sum_{n=1}^{N_{\rm res}}\frac{\Omega'_n}{2}\left((\widehat{Q}'_{n,\Delta_\theta})^2 + (\widehat{P}'_n)^2 - (\widetilde{Q}'_{n,\Delta_\theta})^2 - (\widetilde{P}'_n)^2\right) + \sum_{n=1}^{N_{\rm res}} d'_n\left(\boldsymbol{Q}_{\Delta_\theta}^T\boldsymbol{A}_n^{\theta}\boldsymbol{Q}'_{n,\Delta_\theta} + \boldsymbol{P}^T\boldsymbol{A}_n^{\theta}\boldsymbol{P}'_n\right), \tag{9}$$

where the last term involves the bilinear couplings between the effective mode and the residual modes, recast in terms of the vectors $\boldsymbol{Q}_{n,\Delta_\theta}^T = (\widehat{Q}_{n,\Delta_\theta}, \widetilde{Q}_{n,\Delta_\theta})$ and $\boldsymbol{P}_n^T = (\widehat{P}_n, \widetilde{P}_n)$ that contain the real and tilde components of the coordinates and momenta for the nth residual mode (and corresponding vectors for the effective mode in the absence of the index n). The matrix $\boldsymbol{A}_n^{\theta}$ is the outer product of the transformation coefficient vectors $(\boldsymbol{a}_n^{\theta})^T = (\cosh(\theta_n), \sinh(\theta_n))$ in the mode subspaces,

$$\boldsymbol{A}_n^{\theta} = \boldsymbol{a}^{\theta} \otimes \boldsymbol{a}_n^{\theta} = \begin{pmatrix} \cosh(\theta)\cosh(\theta_n) & \sinh(\theta)\cosh(\theta_n) \\ \cosh(\theta)\sinh(\theta_n) & \sinh(\theta)\sinh(\theta_n) \end{pmatrix}. \tag{10}$$

In Eq. (44) of Paper I,[28] the resulting coupling terms are written out explicitly.

Finally, the second reservoir, pertaining to the torsional mode, is not thermalized since its function is mainly to remove a large amount of excess energy carried by the torsional mode as a result of the passage through the conical intersection,

$$\widehat{H}_{\rm res}^{(\phi)}(\widehat{\phi},\{\widehat{Q}''_n\}) = \sum_{j=1}^{N_\phi}\frac{\omega_n}{2}(\widehat{P}''_n)^2 + \frac{\omega_n}{2}\left(\widehat{Q}''_n - \frac{c_n}{\omega_n}(\widehat{\phi} - \phi_0)\right)^2 \quad \text{with } \phi_0 = 0. \tag{11}$$

In the quantum dynamical calculations reported in the following, the Hamiltonian of Eq. (5) is adapted to two parameterizations of the environmental spectral densities for the $(Q,\{Q_n\})$ dependent part of the Hamiltonian—i.e., "fast" vs "slow" solvent environments; see Sec. IV D of Paper I[28] and the following discussion.

III. QUANTUM DYNAMICAL CALCULATIONS

The thermal Hamiltonian of Eq. (5) with the multiplicative neural network potential of Eq. (4) are employed in quantum dynamical simulations, for varying numbers of NN nodes, from $N_{\rm NN} = 15$ to $N_{\rm NN} = 35$. The number of vibrational degrees of

freedom included in the calculations reaches 100–200 modes due to the discretization of the local reservoirs and the duplication of the thermalized subspaces. While the addition of the tilde modes within the TFD treatment increases the numerical effort of the calculations, the key advantage of the TFD approach is that only a single propagation run is needed to represent ensemble effects. Accurate wavefunction propagation for this number of modes can be carried out by tensor network methods, specifically the ML-MCTDH method,[13–16] as detailed in the following. Among various tensor network schemes, ML-MCTDH is a hierarchical method belonging to the so-called tree tensor network class, which is especially suited to the hierarchical representation of the present model.

In the following, we first summarize the setup for the ML-MCTDH calculations (Sec. III A) and then briefly report on the discretization scheme employed for the local reservoirs (Sec. III B).

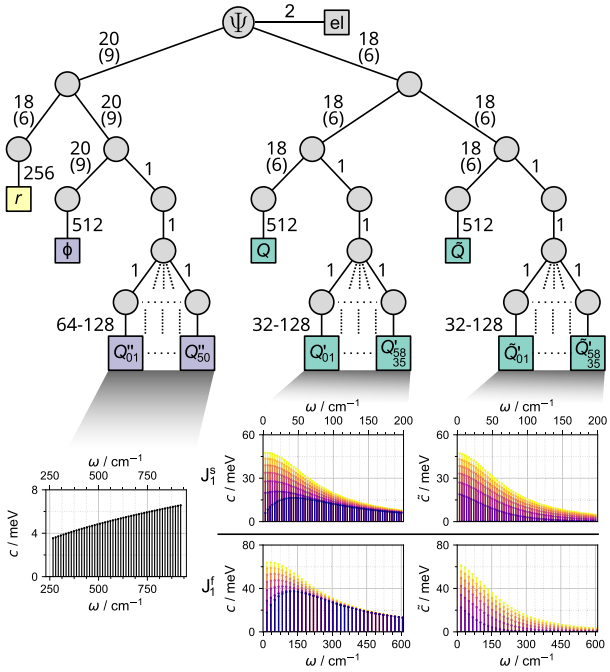

FIG. 2. Multi-layer tree structure of the ML-MCTDH wavefunction. The hierarchical structure of the tree is detailed in the text. The first layer comprises an electronic particle, as well as two vibrational particles grouping together (r, ϕ) vs $(Q, \widetilde{Q})$ and their respective local reservoirs. In the second layer, sub-branches are defined for the vibronically active modes vs their local reservoirs; this applies to the torsional mode ϕ and its local reservoir $\{Q_n''\}$ and analogously to the collective bath mode Q coupled to its reservoir $\{Q_n'\}$, along with the corresponding tilde modes, i.e., mode $\widetilde{Q}$ coupled to the reservoir $\{\widetilde{Q}_n''\}$. In the lower panels, discretized spectral densities for the local baths are shown, including two types of residual SD's, i.e., $J_1^s(\omega)$ and $J_1^f(\omega)$, corresponding to a "slow" vs "fast" environment. [Note that coefficients $c_n = d_n \cosh(\theta_n)$ and $\widetilde{c}_n = d_n \sinh(\theta_n)$ are shown, cf. Eqs. (9) and (10).] In the graphical tree representation, the circles represent nodes, whereas the rectangles represent primitive basis functions of the electronic mode and all the vibrational modes. The numbers next to the lines connecting the nodes indicate the number of SPFs; the numbers in brackets correspond to a complementary, reduced setup, as discussed in the text. The numbers next to the lines connecting a node and a mode indicate the number of primitive basis functions. In cases where the number of primitive basis functions varies for different simulation conditions, the maximum and minimum numbers are indicated.

A. ML-MCTDH calculations

ML-MCTDH calculations are carried out within the extended Hilbert space defined by the TFD wave function. Figure 2 presents a graphical illustration of the wavefunction in terms of a multi-layered tree structure. The uppermost layer takes a standard MCTDH form in a single-set[12] form

$$|\Psi(\phi, r, Q, \{Q_n'\}, \{\widetilde{Q}_n'\}, \{Q_n''\}, t)\rangle = \sum_{m=1}^{2} \sum_{J_1^{(1)}}^{N_1^{(1)}} \sum_{J_2^{(1)}}^{N_2^{(1)}} A^{(1)}_{J_1^{(1)}, J_2^{(1)}, m}(t)$$
$$\Phi^{(1)}_{J_1^{(1)}}(r, \phi, \{Q_n''\}, t) \Phi^{(1)}_{J_2^{(1)}}(Q, \widetilde{Q}, \{Q_n'\}, \{\widetilde{Q}_n'\}, t) |D_m\rangle, \quad (12)$$

where $A^{(1)}_{J_1^{(1)}, J_2^{(1)}, m}$ denotes a multi-index for the first-layer coefficients, $|D_m\rangle$ represent the diabatic (RDS) electronic states, and the first-layer configurations $\Phi_{J_j^{(1)}}$ group together different sets of coordinates: That is, $\Phi_{J_1^{(1)}}$ depends on the modes (r, ϕ) and the local reservoir modes $\{Q_n''\}$ acting on the torsional mode, while $\Phi_{J_2^{(1)}}$ combines the collective mode Q with its thermal reservoir modes $\{Q_n'\}$ and $\{\widetilde{Q}_n'\}$.

These first-layer configurations are in turn expanded in second-layer quantities; for example, the first-layer particle $\Phi_{J_1^{(1)}}$ is expressed as a sum over products of second-layer particles,

$$\Phi^{(1)}_{J_1^{(1)}}(r, \phi, \{Q_n''\}, t) = \sum_{J_1^{(2)}}^{N_1^{(2)}} \sum_{J_2^{(2)}}^{N_2^{(2)}} A^{(2)}_{J_1^{(2)} J_2^{(2)}}(t) \Phi^{(2)}_{J_1^{(2)}}(r, t) \Phi^{(2)}_{J_2^{(2)}}(\phi, \{Q_n''\}, t) \quad (13)$$

and the procedure is iteratively continued to higher layers. Overall, a five-layer form of the wavefunction is employed, as illustrated in Fig. 2. In the final layer, the intermediate so-called single-particle functions (SPF's) are expressed in a primitive basis, using discrete variable representations (DVR's).[12] For the (ϕ, r, Q) modes, a fast Fourier transform (FFT) type DVR is used with 256 or 512 DVR points, while the reservoir modes are represented using a harmonic oscillator (HO) DVR, with 32–128 DVR points.

Initial conditions were adapted to an adiabatic initial state on the upper (S_1) potential, with a slightly pre-twisted torsional configuration at $\phi = 0.5$ rad, and $r = 1.5$ Å and $Q = -\Delta$, as shown in Fig. 1(b), where the value of Δ depends on the solvent model.

Correlations are comparatively strong in the present system due to the anharmonicity of the potentials defined by the conical intersection topology. As a result, the number of single-particle functions (SPF's), i.e., $N_j^{(k)}$ in Eqs. (12) and (13), was chosen up to 20 in the first layers, as shown in Fig. 2 (see Sec. S1 in the supplementary material for details). Conversely, the local reservoirs turned out to be well-described by single configurations, i.e., Hartree-type sub-branches; see the discussion in Sec. III B. The numbers of SPF's indicated in the multi-layer tree of Fig. 2 were adjusted to reach maximum natural orbital populations around a threshold of 2×10^{-2}. In a complementary setup (indicated in brackets in Fig. 2), the SPF numbers are reduced to 6–9 in the upper layer, leading to

maximum natural orbital populations around 9×10^{-2}, while keeping the dynamical evolution qualitatively unchanged (see Sec. S1.1 in the supplementary material). This setup is used in combination with a diabatic–adiabatic transformation (see Sec. IV A) whose cost depends on the number of expansion coefficients.

Overall, calculations were performed for the two-state system with up to 170 vibrational modes, using the ML-MCTDH approach as implemented in the Heidelberg MCTDH package.[56] All calculations were carried out on 2.6 GHz Intel Xeon E5-2690v4 processors using a single thread.

B. Local reservoirs

The construction of the discretized local reservoirs shown at the bottom of the hierarchical tree structure of Fig. 2 follows from the Hamiltonians $\widehat{H}_{\rm res}^{(\phi)}$ of Eq. (11) and $\widehat{H}_{T,\rm res}^{(Q)}$ of Eq. (9).

The local reservoir acting on the torsional mode is meant to absorb a significant part of the excess energy imparted to the torsion during the passage through the conical intersection. Thermalization of this local reservoir is, therefore, not of importance, and the main property of the reservoir is its capacity for resonant energy transfer. A phenomenological environment suffices for this purpose, such that an Ohmic spectral density[57] is used in a discretized representation,

$$J_\phi(\omega) = \frac{\pi}{2}\sum_{n_\phi=1}^{N_\phi} c_{n_\phi}^2 \delta(\omega - \omega_{n_\phi}), \tag{14}$$

where the couplings c_{n_ϕ} are chosen such as to reproduce an Ohmic SD, $J_\phi(\omega) = \gamma_\phi \omega$, where γ_ϕ is the friction coefficient associated with the damping of the ϕ mode, taken to be $\gamma_\phi^{-1} = 50$ fs in the simulations reported in the following. The bilinear couplings are given as $c_{n_\phi} = \sqrt{(2/\pi)\gamma_\phi \Delta_\phi \omega_{n_\phi}/\omega_\phi}$, where Δ_ϕ is the equidistant frequency grid spacing, ω_{n_ϕ} are the discretized frequencies, and ω_ϕ is the harmonic approximation to the torsional ground-state potential. The reference position $\phi_0 = 0$ is assumed in Eq. (11). Further details are specified in Sec. S1.2 in the supplementary material.

Conversely, the local reservoirs acting on the effective mode Q according to $\widehat{H}_{T,\rm res}^{(Q)}$ of Eq. (9) result from the effective-mode transformation detailed in Paper I.[28] The underlying solvent spectral density is of quantum overdamped type; see Eq. (19) in Paper I,[39]

$$J(\omega) = 4\lambda \frac{\omega \Lambda^3}{(\omega^2 + \Lambda^2)^2}. \tag{15}$$

The parameters λ and Λ can be determined from the collective-mode frequency and displacement available from the NN fit, as detailed in the Appendix. (However, in the present study, a known reference SD parameterization is used, as detailed in Sec. S1.3 in the supplementary material.)

The associated residual spectral densities $J_1(\omega)$ are shown in Fig. 2(b) of Paper I[28] and their formal construction is detailed in Sec. S3.1 in the supplementary material of Paper I.[28] As can be inferred from Fig. 2, two residual reservoirs are defined, which interact with the collective mode (Q) and its tilde counterpart $(\widetilde{Q})$, respectively. The discretized representation of these reservoirs conforms to the thermal SD's[50] (see Paper I[28]),

$$J_1^\theta(\omega) = \frac{\pi}{2}\sum_n (c_n^T)^2 \delta(\omega - \omega_n) \tag{16}$$

and

$$\widetilde{J}_1^\theta(\omega) = \frac{\pi}{2}\sum_n (\widetilde{c}_n^T)^2 \delta(\omega - \omega_n), \tag{17}$$

with the thermal vibronic couplings $c_n^T = c_n \cosh\theta_n$ and $\widetilde{c}_n^T = c_n \sinh\theta_n$. In the construction of these discretized residual SD's, an equidistant sampling of the reference SD's of Eq. (15), as described in Paper I,[28] translates to near-equidistant sampling of the residual SD's, as detailed in Sec. S1.3.2 in the supplementary material.

All local reservoirs turned out to be reasonably well described by the Hartree approximation, with a single configuration, which is essentially due to the low-frequency character of the relevant modes. As discussed in detail in Sec. S3 in the supplementary material, comparative computations were carried out for a correlated description of the local baths, showing that the Hartree approximation yields acceptable accuracy. The Hartree approximation also facilitates the approximate diabatic-to-adiabatic transformation described in Sec. IV A.

One should note that the sampling procedure for the local reservoirs was not optimized and (near-)equidistant sampling is not generally an efficient strategy. However, the disadvantages of the sampling scheme are largely compensated for by the Hartree approximation, which makes the propagation robust with respect to the size of the local reservoirs. In future work, improved sampling schemes for the residual reservoirs will be employed, notably resulting from hierarchical effective-mode chains with suitable truncation criteria.[58–62] Related chain-mapping schemes have more recently been adapted to the TFD representation,[63,64] and alternative low-rank discretization strategies have been explored.[65,66] In addition, logarithmic sampling can be useful for Ohmic and sub-Ohmic spectral densities.[67] In future applications, the present approach will doubtlessly benefit from various improved SD sampling strategies that are gaining ground in conjunction with tensor network methods.[68,69]

IV. ANALYSIS METHODS

For the purpose of analysis of the quantum dynamical simulations, several specific methods were implemented, notably an approximate diabatic-to-adiabatic transformation (Sec. IV A), the Wigner function[70] representation of selected modes (Sec. IV B), and the computation of the reduced single-particle density for the thermalized modes (Sec. IV C).

A. Diabatic-to-adiabatic transformation

Since the diabatic wavefunction densities obtained in the NN/RDS representation differ significantly from their adiabatic counterparts, a diabatic-to-adiabatic transformation is carried out in order to obtain time-evolving adiabatic state populations. Even though the overall number of degrees of freedom is large, the collective-mode formulation simplifies the situation since the

diabatic-to-adiabatic transformation is a function of the coordinates that are coupled to the electronic subsystem, i.e., (r, ϕ, Q). A numerically exact diabatic-to-adiabatic transformation is in principle feasible in three dimensions, but the transformation is carried out in the primitive (DVR) representation and remains highly demanding for our system. Therefore, we implemented an approximate transformation that is now briefly described and presented in further detail in Sec. S2 in the supplementary material.

Given that the dynamics in the collective coordinate Q is simpler than in the coordinates (r, ϕ), an approximation is made with respect to the DVR representation of this coordinate. We proceed as follows, within a Hartree representation for the local baths, which are not coupled to the electronic subsystem. The diabatic reduced density matrix $\{\rho_{nm}(\phi, r, Q)\}$ is constructed in the DVR representation, based on the ML-MCTDH form of Eq. (12). Subsequently, a renormalized DVR representation is introduced where a limited number of $s = \{1, 3, \ldots, 9\}$ DVR slices are taken for the collective mode Q, while the representation of the modes (ϕ, r) remains unchanged. As shown in Sec. S2 in the supplementary material, this "DVR(s)" scheme can be shown to give consistent results for small s values, and acceptable accuracy is already obtained for $s = 1$, which corresponds to a mean-field approximation where the distribution of the Q mode is approximated in terms of its expectation value $\langle Q \rangle$.

B. Reduced density matrices and Wigner functions

In our analysis in the following, reduced single-particle densities will be shown for selected degrees of freedom, computed within the ML-MCTDH setup,

$$\widehat{\rho}^{(\kappa)}(t) = \underset{\text{el}}{\text{Tr}} \underset{\kappa' \neq \kappa}{\text{Tr}} \{|\Psi(t)\rangle\langle\Psi(t)|\}, \tag{18}$$

where $|\Psi(t)\rangle$ is the ML-MCTDH wavefunction of Eq. (12), and the κth degree of freedom is singled out while the trace is taken over all vibrational modes $\kappa' \neq \kappa$, and over the electronic degrees of freedom (hence, the result corresponds to state-averaged quantities). The above-mentioned trace operation translates to overlaps of single-hole densities in the tensor representation of the ML-MCTDH wavefunction.[13] The quantity $\widehat{\rho}^{(\kappa)}(t)$ as defined in Eq. (18) is a reduced density operator, whose matrix elements in the DVR representation are given as

$$\rho^{(\kappa)}(x_\kappa, x'_\kappa, t) = \langle \chi(x_\kappa)|\widehat{\rho}^{(\kappa)}(t)|\chi'(x'_\kappa)\rangle, \tag{19}$$

where the diagonal matrix elements yield mode-specific local densities, $\rho^{(\kappa)}(x_\kappa, t) = \langle \chi(x_\kappa)|\widehat{\rho}^{(\kappa)}(t)|\chi(x_\kappa)\rangle$.

Based on the coordinate representation Eq. (19) of the reduced density, a phase-space picture can be introduced by a transformation yielding the Wigner function.[70] The Wigner function is a quasi-probability distribution, which adopts negative values in phase space regions where quantum interference appears. This distribution is, therefore, highly informative to represent the passage through a conical intersection. Here, we use the Wigner transformation of the reduced densities of Eq. (19) in order to compute the Wigner function $W^{(\kappa)}$,

$$W^{(\kappa)}(q_\kappa, p_\kappa, t) = \frac{1}{2\pi} \int \mathrm{d}r_\kappa \, e^{-ip_\kappa r_\kappa} \rho^{(\kappa)}\left(q_\kappa + \frac{r_\kappa}{2}, q_\kappa - \frac{r_\kappa}{2}; t\right), \tag{20}$$

where $q_\kappa = \frac{1}{2}(x_\kappa + x'_\kappa)$ and $r_\kappa = x_\kappa - x'_\kappa$ are sum and difference coordinates, and the phase-space momentum p_κ appears as the conjugate Fourier variable of the difference coordinate r_κ (also see Sec. S3 in the supplementary material). In the following, we will specifically show the Wigner transform of the torsional mode ϕ (see Sec. V C).

C. Reduced density matrices in the TFD representation

For the thermalized modes, the computation of reduced single-particle densities is complicated by the iBT variant of the TFD approach that is employed in this work (see Sec. II C). As mentioned above and as detailed in Paper I,[28] in the iBT variant, the thermal Hamiltonian of Eq. (5) is constructed by shifting the Bogoliubov transformation and, hence, the temperature dependence, from the initial condition into the Hamiltonian.[50,54,55] While this offers the great advantage of using zero-temperature initial conditions, the computation of the thermalized reduced mode densities necessitates a back-transformation. As detailed in Sec. S4 in the supplementary material and in Ref. 55, the primary object is now a two-mode density in the combined real/tilde subspace,

$$\widehat{\rho}^{(\kappa,\widetilde{\kappa})}(t) = \underset{\text{el}}{\text{Tr}} \underset{\chi \neq \kappa,\widetilde{\kappa}}{\text{Tr}} \left\{ \widehat{T}_\Delta^\dagger |\Psi_T(t)\rangle\langle\Psi_T(t)| \widehat{T}_\Delta \right\}, \tag{21}$$

where the trace is taken over all modes $\chi \neq \kappa, \widetilde{\kappa}$ and $\widehat{T}_\Delta = e^{-i\widehat{G}_\Delta(\theta)}$ is a shifted Bogoliubov transformation for a displaced reference state; see Eq. (37) of Paper I.[28] From this, the physical single-particle density is obtained as[55]

$$\begin{aligned} \rho^{(\kappa)}(Q, t) = \int d\widetilde{Q} \, \rho^{(\kappa,\widetilde{\kappa})} \big(& Q_{\Delta'_\theta} \cosh(\theta) - \widetilde{Q}_{\Delta'_\theta} \sinh(\theta), \\ & - Q_{\Delta'_\theta} \sinh(\theta) + \widetilde{Q}_{\Delta'_\theta} \cosh(\theta) \big), \end{aligned} \tag{22}$$

where $Q_{\Delta'_\theta} \equiv Q + \Delta'_\theta$, with $\Delta'_\theta = \Delta(e^\theta - 1)$. As can be seen from the arguments of the two-particle density $\rho^{(\kappa,\widetilde{\kappa})}$ in Eq. (22), the real and tilde modes are mixed, which complicates taking the trace over the tilde subspace (see Ref. 55 for a detailed discussion). In the present context, the reduced density is constructed by interpolation in the DVR representation, as detailed in Sec. S4 in the supplementary material.

The associated expectation value of the thermalized mode is given as

$$\langle Q \rangle = \langle Q_{\Delta_\theta} \rangle \cosh(\theta) + \langle \widetilde{Q}_{\Delta_\theta} \rangle \sinh(\theta), \tag{23}$$

where Q_{Δ_θ} and $\widetilde{Q}_{\Delta_\theta}$ are defined below in Eq. (8). For zero displacement, this expression reduces to Eq. (23) in Ref. 54.

V. THERMOFIELD DYNAMICS AT THE PSB CONICAL INTERSECTION

In this section, results of ML-MCTDH calculations are discussed based on the wavefunction setup encoded in the multi-layer tree of Fig. 2. As can be anticipated from Fig. 1, the dynamical evolution is expected to show the approach to the conical intersection seam at $\phi = \pi/2$, followed by nonadiabatic passage through

the conical intersection. The time scale of the approach to the CI is determined by the vibronically active coordinates, i.e., the coupling mode ϕ and the tuning modes r and Q, where the latter is an effective environmental coordinate as discussed above. Notably, the intrinsic time scale of the inertial non-equilibrium dynamics of the solvent can act as a determining factor in the approach to the CI. Due to the extreme anharmonicity at the conical intersection, a complex nonadiabatic dynamics is expected. Furthermore, the excited-state wavepacket carries a significant amount of excess energy, which is partially absorbed by the local baths acting on both the torsional mode and the effective environmental coordinate.

In the following, we first assess the quality of the m-NN based dynamics (Sec. V A) and then address the role of the environmental dynamics in the nonadiabatic passage through the conical intersection (Sec. V B), including a perspective from the Wigner representation (Sec. V C).

A. Quality of m-NN-based dynamics

From the discussion in Paper 1,[28] we recall that the m-NN potentials are in excellent agreement with the reference potentials, such that we expect to obtain a wavepacket dynamics that is in good agreement with the reference dynamics, too. Figure 3 illustrates that this is indeed the case, using an NN fit with $N_{\mathrm{NN}} = 35$ nodes. The figure shows the time-evolving reduced densities, as defined in Eq. (19), for ML-MCTDH dynamics at zero temperature, based on the "fast" $J^f(\omega)$ spectral density (see Fig. 2). The passage through the CI takes place around $t \simeq 50$ fs and is reflected in a significant spreading of the reduced densities of the three vibronically active modes. The m-NN-based dynamics is in very close agreement with the reference dynamics until the conical intersection is reached and remains in good agreement beyond the passage through the CI. However, the differences between the time-evolving densities show that some deviations occur, which are mainly related to a slight shift of the densities. Apart from this, the overall dynamics is faithfully reproduced by the m-NN potentials.

As detailed in Sec. S5 in the supplementary material, the agreement is somewhat less favorable although, at finite temperature. This is likely due to the LVC approximation made in the construction of the thermal Hamiltonian of Eq. (5), which affects the NN-RDS potentials slightly differently than the reference potential.[37]

As shown in Fig. 4 and further detailed in Sec. S6 in the supplementary material, the scaling of the dynamical calculations using NN approximants with increasing number of nodes is near-linear as a function of N_{NN}, such that dynamical calculations with highly converged m-NN potentials are feasible.

B. Effect of environmental dynamics

Turning to the effects of the environment, we now compare the dynamics induced by the two spectral densities characterized in Paper 1[28] (see Sec. II D). While both of these SDs conform to a Debye-type, quantum overdamped Brownian oscillator form of Eq. (15), $J^s(\omega)$ is more strongly concentrated at low frequencies than $J^f(\omega)$, and hence, $J^s(\omega)$ exhibits a smaller effective-mode frequency ($\Omega_s = 77$ cm^{-1}) than $J^f(\omega)$ ($\Omega_f = 229$ cm^{-1}), hence the designations as "slow" vs "fast" solvents. In Fig. 2, the discretized residual SDs are shown, in line with Fig. 2 of Paper I.[28] Both SDs feature a pronounced temperature dependence (see Fig. 2), such that

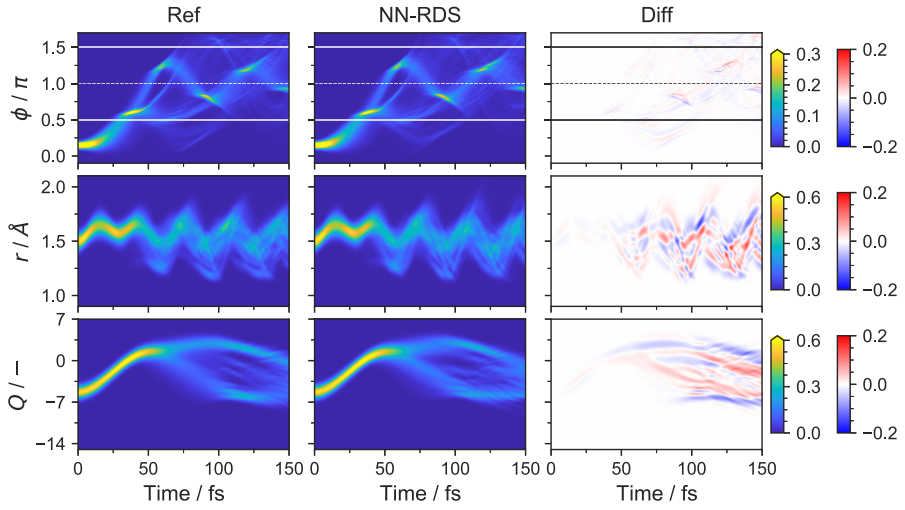

FIG. 3. Based on the setup illustrated in the multi-layer tree of Fig. 2, the dynamical evolution of the reduced densities of the vibronically coupled modes (ϕ, r, Q) is shown at $T = 0$ K for the fast solvent represented by $J^f(\omega)$. Calculations based on the reference potentials[37] (l.h.s. panels) are compared to calculations for the NN-RDS potentials with $N_{\mathrm{NN}} = 35$ (center panels), and the difference is shown in the r.h.s. panels. All calculations are based on the same form of the wavefunction according to Sec. III. It is seen that the NN dynamics is in excellent agreement with the reference dynamics until the passage through the conical intersection around $t \simeq 50$ fs. Upon passage through the CI, the dynamics becomes more complex, leading to more pronounced deviations from the reference dynamics. Mainly, the reduced densities are slightly shifted while the time-evolving structures are very well reproduced throughout. Note the difference in scales for the densities vs differences.

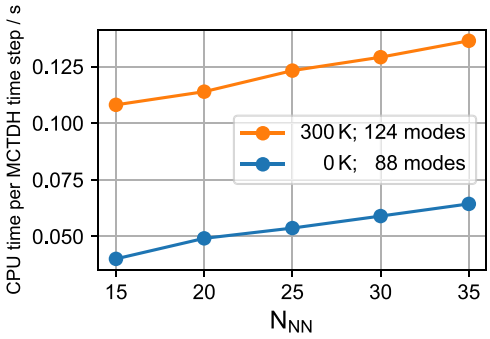

FIG. 4. Time profiling of representative ML-MCTDH simulations at $T = 0$ K and $T = 300$ K, for the fast solvent represented by $J^f(\omega)$, analogous to the dynamics shown in Fig. 5. The average CPU time per ML-MCTDH time step is shown. A near-linear scaling is observed across the relevant range of NN nodes, $N_{NN} = 15, \ldots, 35$.

thermalization of both the collective mode and the residual bath is expected to have a pronounced effect.

Figure 5 shows a comparison between the NN-RDS based dynamics (with $N_{NN} = 15$ nodes), obtained for $J^s(\omega)$ and $J^f(\omega)$, respectively, for a thermalized solvent environment, i.e., including environmental modes $(Q, \{Q'_n\})$ and $(\widetilde{Q}, \{\widetilde{Q}'_n\})$ at $T = 300$ K. We expect pronounced inertial solvent effects since the initial solvent state, equilibrated to the ground-state charge distribution ($Q = -\Delta$ in Fig. 1), is going to adjust to the excited-state charge distribution.

In the l.h.s. panels, the dynamics for the fast SD, $J^f(\omega)$, is shown, analogously to Fig. 3, now accompanied by diabatic and approximate adiabatic populations shown in panels (a) and (b), respectively. As mentioned above, the passage through the conical intersection region happens around $t \simeq 50$ fs, leading to a dominant population of the S_0 ground state, while a partial excited-state population is retained. Panels (c)–(e) show the reduced densities pertaining to the modes (ϕ, r, Q), similarly to Fig. 3. The time-evolving density of the torsional mode, in panel (c), shows that the wavepacket splits up when the conical intersection is encountered at $\phi = \pi/2$, followed by oscillatory motion around the local S_0 minimum at $\phi = \pi$. Meanwhile, the dynamics of the tuning mode r depicted in panel (d) exhibits pronounced oscillations when approaching the conical intersection, in line with Fig. 1 and in agreement with experimental observations on retinal type systems.[71] The collective mode Q, shown in panel (e), exhibits a slower inertial dynamics, but its evolution from the initial condition $Q = -\Delta$ toward excited-state equilibration ($Q = \Delta$) is critical in order to reach the conical intersection seam, as can be inferred from Fig. 1. The reduced densities of both tuning modes (r, Q) spread out but overall remain more compact than the torsional density following the passage through the CI. Panel (f) illustrates that energy dissipation plays a crucial role, and the net amount of excess energy dissipated into both local reservoirs (J_1 and J_ϕ) is around 2 eV. In fact, J_ϕ is essential to induce the observed population inversion of the adiabatic states; also see Sec. S7 in the supplementary material where different simulation conditions are discussed and the energy exchange is addressed in further detail.

Analogously, the r.h.s. panels of Fig. 5 show the dynamics for the "slow" SD, $J^s(\omega)$, which differs in several important respects from the previous case. First, panels (g) and (h) show that the passage through the conical intersection region occurs later, around $t = 90$ fs, since the slower dynamics of the collective environmental mode is the rate limiting step for the encounter of the CI seam (see Fig. 1). Next, panel (i) shows that the torsional density settles down at $\phi = 0$, i.e., the isomerization quantum yield is extremely small, while it is large in the case of $J^f(\omega)$. While the dynamics of the r mode in panel (j) remains similar as in the $J^f(\omega)$ case, the slowing down of the Q mode, illustrated in panel (k) must be the reason for the strongly modified directionality of the torsional dynamics. The broadening of the solvent distribution, due to more pronounced thermalization effects, also plays a certain role. As a result, it turns

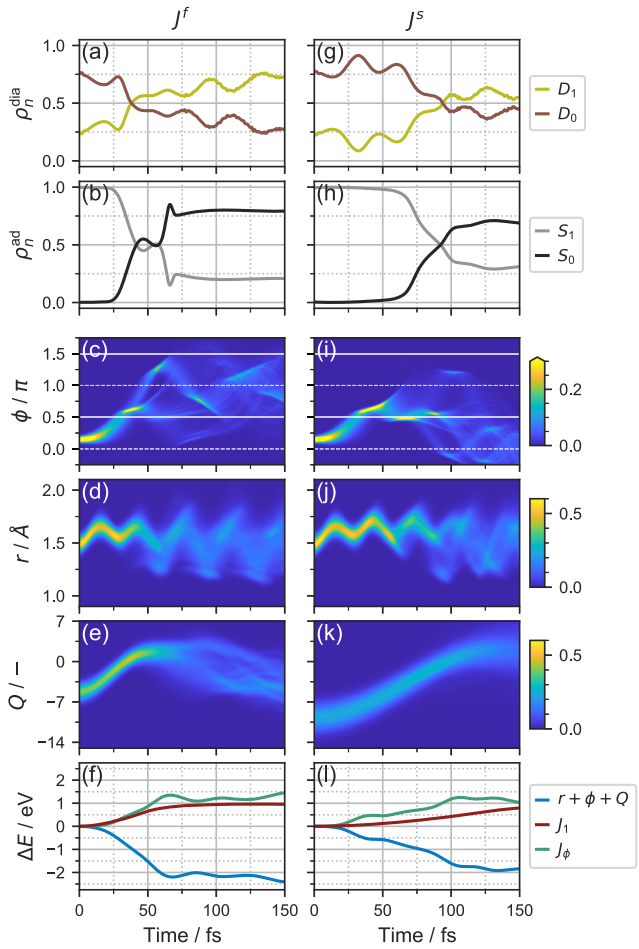

FIG. 5. Comparison between the NN-RDS dynamics induced by the spectral densities $J^f(\omega)$ and $J^s(\omega)$ at $T = 300$ K, with $N_{NN} = 15$ nodes. (a)–(f) Dynamics obtained for the fast solvent $[J^f(\omega)]$, illustrated by (a) the diabatic state populations (ρ_n^{dia}), (b) approximate adiabatic state populations (ρ_n^{ad}) obtained with the reduced SPF setup as explained in the text, (c) the reduced density of the torsional mode, (d) the reduced density of the r mode, (e) the reduced density of the collective Q mode, and (f) relative subspace energies for the vibronically active modes (ϕ, r, Q) and the local baths (J_1^f, J_ϕ). (g)–(l) Corresponding dynamics obtained for the slow solvent $[J^s(\omega)]$.

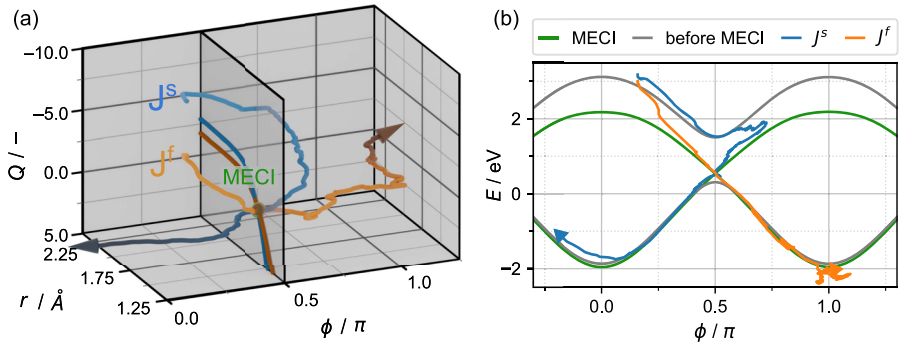

FIG. 6. For the dynamics shown in Fig. 5, panel (a) shows the time-evolving expectation values $(\langle\phi\rangle, \langle r\rangle, \langle Q\rangle)$ for the fast solvent SD $[J^f(\omega)]$ and the slow solvent SD $[J^s(\omega)]$, respectively. At the center, the CI seam is shown in the (r, Q) plane at $\phi = \pi/2$. The mean paths for both solvent realizations approach the MECI and from there proceed either toward $\phi = 0$ [for $J^f(\omega)$] or $\phi = \pi$ [for $J^f(\omega)$]. (b) Projection of the mean paths onto 1D PES cuts along the torsional mode before and at the MECI, illustrating the direct passage through the CI in the case of $J^f(\omega)$ and the delayed passage in the case of $J^s(\omega)$. In the latter case, a momentum reversal occurs before the CI seam is reached, leading to a non-reactive outcome. Note that the present representation serves for illustration and does not faithfully describe the net energy loss of the vibronically active coordinates, which amounts to about 2 eV; see Figs. 5(f) and 5(l).

out that due to the delayed passage through the conical intersection induced by the slower environmental mode, prolonged excited-state torsional motion in the S_1 state occurs, which leads to a momentum reversal and, hence, a non-reactive path leading back to the $\phi = 0$ local minimum of the S_0 ground state. Energy dissipation again amounts to ~2 eV (panel l), even though the onset is slower as expected.

The dynamical scenarios pertaining to the $J^s(\omega)$ vs $J^f(\omega)$ cases are sketched in Fig. 6. Panel (a) shows time-evolving expectation values for all vibronically active modes $(\langle\phi\rangle, \langle r\rangle, \langle Q\rangle)$, illustrating the initial approach to the MECI, followed by ground-state dynamics which leads either to the *cis* $(\phi = 0)$ or *trans* $(\phi = \pi)$ minimum. While in the case of $J^f(\omega)$, the torsional motion in S_1 leads immediately to the MECI, the slow $J^s(\omega)$ solvent dynamics causes the torsion to evolve on the S_1 surface and approach the MECI with inverted momentum. This is sketched in panel (b), which highlights the excursion on the upper PES prior to reaching the MECI in the case of $J^s(\omega)$. Clearly, the effective solvent mode controls the passage through the conical intersection in these dynamical situations and influences not only the time of passage through the intersection but also the isomerization quantum yield.

C. Wigner representation

Complementary to the above-mentioned discussion, further insight into the nonadiabatic dynamics is obtained in the Wigner representation;[70] see Sec. IV B. In Fig. 7, the two types of dynamics induced by J^s and J^f, respectively, at $T = 300$ K are shown in a two-dimensional phase space representation for the torsional mode, (ϕ, p_ϕ).

In the case of J^f, it is seen that the torsional wavepacket separates into two components around $t = 48$ fs. These feature coherent superposition effects as can be inferred from the negative components of the Wigner function. Comparison with the dynamics at $T = 0$ K (see the supplementary material including an animation of the wavefunction evolution) shows that these interference effects are less pronounced in the thermalized state, but they are still present. Concerted, parallel oscillatory motion of these components is observed, until the wavepacket starts to settle down around the local S_0 minimum at $\phi = \pi$.

The dynamics of the slower solvent, represented by $J^s(\omega)$, shows wavepacket splitting at a later point in time, around $t = 72$ fs. As explained above, this delay is entirely due to the slower solvent motion, which acts as a dynamical barrier and causes the torsional wavepacket to approach the conical intersection from a different angle. In the Wigner representation, a localized density spot at $\phi = \pi/2$ is observed, in addition to oscillatory components that feature opposite momenta. The density component at $\phi = \pi/2$ can be related to a metastable twisted diradical configuration[72] in the proximity of the CI seam, preceding decay along the seam line. This transient is discernible in the coordinate domain too; see Fig. 5(i). Finally, the wavepacket converges toward the S_0 minimum at $\phi = 0$, in a non-reactive photoreaction.

For further illustration, the supplementary material contains multimedia files illustrating Wigner function and Husimi function[70] evolution, as well as the approximate adiabatic wavepacket evolution. In addition, Sec. S8 in the supplementary material presents comparisons of the dynamics under the NN-RDS vs reference potentials, and Sec. S9 further illustrates the Wigner/Husimi function evolution and adiabatic probability densities.

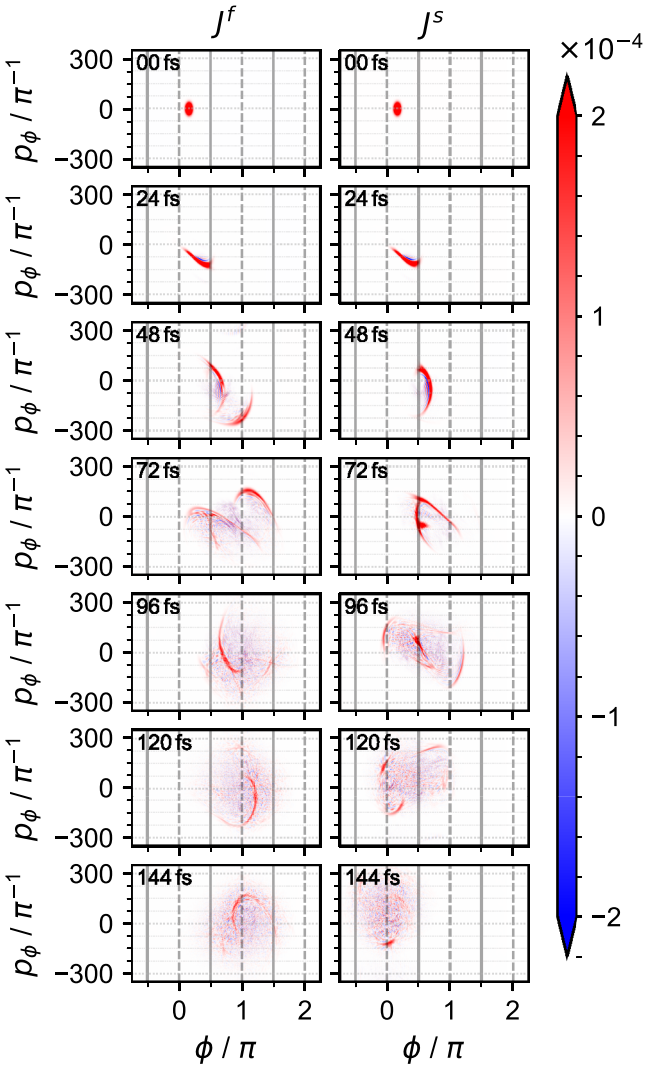

FIG. 7. Complementary to Fig. 5, snapshots of the Wigner representation are shown for the dynamics induced by the spectral densities $J^f(\omega)$ and $J^s(\omega)$ at $T = 300$ K. The phase space perspective illustrates the bifurcation of the wavepacket at the conical intersection and the momentum reversal in the case of the delayed passage through the CI in the case of the slow solvent $[J^s(\omega)]$. See the text for a detailed discussion.

VI. DISCUSSION AND CONCLUSIONS

The present study demonstrates that multiplicative neural network potentials combined with tensor network methods for quantum propagation are highly suitable to represent vibronic dynamics in non-equilibrium environments. A key feature of the present m-NN construction is the inclusion of collective environmental coordinates on par with intramolecular vibrations, beyond the conventional linear vibronic coupling model. A second key element is the thermofield dynamics approach, which permits thermalization of the environment within a single wavefunction realization, in the absence of computationally demanding ensemble averages. The hierarchical structure of the ML-MCTDH wavefunction ansatz fully accommodates the inclusion of local reservoirs acting upon vibronically active modes. These reservoirs play an important role in the dynamics, both regarding the initial thermalization of the subsystem and regarding the absorption of the large excess energy that arises in a photochemical conversion process. If dissipation is insufficient, the remaining excess energy can lead to rotational motion involving the periodic conical intersections, as has been observed for small chromophores in QM/MM-based simulations[73] (also see Sec. S8 in the supplementary material).

The construction of thermal local reservoirs according to the TFD approach is particularly convenient when employing a TFD formulation, which refers to a Bogoliubov transformed (iBT) thermal Hamiltonian.[49,50,54] In Paper I,[28] we have shown how this Hamiltonian can be adapted to an effective-residual mode representation of the discretized spectral density. As a result, an augmented vibronic coupling model is obtained, where the vibronically active effective modes are duplicated and coupled to respective residual reservoirs, which also contain a duplicated number of modes. In the context of tensor network schemes, the augmented number of modes is straightforward to accommodate. Future applications will address efficient sampling schemes for structured residual reservoirs, relating to hierarchical chain representations[58–62] and related approaches that account for thermalization.[63–66,68]

Despite the advantages of the iBT approach, the present application also illustrates that this representation is less convenient when defining reduced densities, as mentioned in Sec. IV C and further discussed in Ref. 55. More efficient approaches also will be explored in this context.

The conical intersection topology under study provides a striking example of environmental effects since the slow environmental mode not only determines the time scale of approach toward the conical intersection but also steers the dynamics of other modes at the CI topology. In the model systems we examined, the outcomes of the photochemical reaction in different solvents range from minimal to maximal photoisomerization yields. The presence of the environmental mode can lead to changes in the excited-state dynamics preceding the nonadiabatic events, for example, relating to torsional motion in the upper cone region. This could also include transient stabilization of twisted diradical configurations, which have been discussed in a related context,[72] as well as changes of the conical intersection topology, e.g., from peaked to sloped.[6,74]

While the present simulations are meant to be a proof-of-principle study based on a reference potential,[37] the next steps are applications of the present approach to electronic structure based datasets. As discussed in Paper I,[28] different levels of treatment can be envisaged, from NN fitting for the isolated chromphore combined with a solvent spectral density, to QM/MM based sampling for the chromophore-plus-environment system. In the latter case, the reduction of atomistic data to collective modes—e.g., energy gap coordinates—is a key step.

Finally, the present approach can be straightforwardly extended to other vibronic coupling systems, notably multi-chromophoric systems[75] and various types of lattice Hamiltonians. In a different context, machine learning approaches have already been combined with the collective-mode concept,[76] which could prove highly useful in the context of vibronic potentials and dynamics.

SUPPLEMENTARY MATERIAL

See the supplementary material for details on the ML-MCTDH calculations including details on the spectral density discretization (Sec. S1), the approximate adiabatic–diabatic transformation that is employed (Sec. S2), the reduced phase-space analysis via Wigner and Husimi functions (Sec. S3), the computation of thermalized reduced densities (Sec. S4), convergence analysis for the NN potentials (Sec. S5), time profiling of the ML-MCTDH calculations (Sec. S6), analysis of the energy redistribution during the dynamics (Sec. S7), comparative dynamics in the NN-RDS vs reference representation (Sec. S8), and various 2D illustrations of reduced densities and their phase-space analogs (Sec. S9). The supplementary material also contains movies illustrating the passage through the conical intersection.

ACKNOWLEDGMENTS

The authors acknowledge the financial support from the Leverhulme Trust Research Project under Grant No. RPG-2023-078. Furthermore, we thank Werner Koch for his contributions to the implementation of the multiplicative neural network approach.

AUTHOR DECLARATIONS

Conflict of Interest

The authors have no conflicts to disclose.

Author Contributions

Bartosz Błasiak: Conceptualization (equal); Data curation (lead); Formal analysis (equal); Investigation (equal); Methodology (equal); Software (lead); Validation (lead); Visualization (supporting); Writing – original draft (supporting); Writing – review & editing (supporting). **Dominik Brey**: Conceptualization (supporting); Data curation (supporting); Formal analysis (supporting); Investigation (supporting); Methodology (supporting); Software (supporting); Validation (supporting); Visualization (lead); Writing – review & editing (supporting). **Rocco Martinazzo**: Conceptualization (supporting); Formal analysis (supporting); Investigation (supporting); Methodology (supporting); Writing – original draft (supporting); Writing – review & editing (supporting). **Irene Burghardt**: Conceptualization (equal); Formal analysis (equal); Funding acquisition (lead); Investigation (equal); Methodology (equal); Project administration (lead); Resources (lead); Supervision (lead); Validation (supporting); Visualization (supporting); Writing – original draft (lead); Writing – review & editing (lead).

DATA AVAILABILITY

The data that support the findings of this study are available from the corresponding author upon reasonable request.

APPENDIX: CONSTRUCTION OF THERMALIZED LOCAL RESERVOIR

Within the present setup, the NN potentials of Eq. (4) obtained as described in Paper I,[28] describe the collective environmental mode, but they do not directly inform about the residual environment which is here defined in terms of a residual spectral density, see Fig. 2. However, given the constraint that the collective mode and the residual bath taken together must conform to the quantum overdamped spectral density of Eq. (15), we can use the following analytical relations between the SD parameters and the collective-mode frequency and displacement:

$$\Omega = \frac{2}{\pi C^2}\int_0^\infty d\omega\ \omega J(\omega) = \frac{\pi\Lambda}{2}$$
$$\Delta = 4\left(\frac{\lambda}{\Lambda\pi^3}\right)^{1/2}. \tag{A1}$$

Hence, the parameters λ and Λ of the quantum overdamped spectral density can be determined from the collective-mode parameters Ω and Δ which are in turn available from the NN fit at a suitable reference geometry. Typically, the ground-state (S_0) minimum is chosen as reference geometry (see Table I of Paper I[28]); however, in the present study, the frequencies and displacements for the solvent collective mode are derived from the reference SD of Table S3 in the supplementary material (which are in turn in good agreement with the values from Table I of Paper I[28]). In the next step, the residual spectral density $J_1(\omega)$ is determined, which is obtained in terms of a Cauchy transform,[60] or numerically by a coordinate transformation within a discretized representation, where the residual modes are bilinear coupled to the collective mode Q.[32–35] The resulting residual SD's are shown in Fig. 2(b) of Paper I[28] and in the bottom panels of Fig. 2.

REFERENCES

[1] W. Domcke, D. R. Yarkony, and H. Köppel, *Conical Intersections* (World Scientific, 2004).
[2] H. Köppel, W. Domcke, and L. S. Cederbaum, "Multimode molecular dynamics beyond the Born-Oppenheimer approximation," in *Advances in Chemical Physics* (John Wiley & Sons, Ltd, 1984), pp. 59–246.
[3] A. Toniolo, G. Granucci, and T. J. Martínez, "Conical intersections in solution: A QM/MM study using floating occupation semiempirical configuration interaction wave functions," J. Phys. Chem. A **107**, 3822–3830 (2003).
[4] S. Gozem, H. L. Luk, I. Schapiro, and M. Olivucci, "Theory and simulation of the ultrafast double-bond isomerization of biological chromophores," Chem. Rev. **117**, 13502–13565 (2017).
[5] C. Punwong, J. Owens, and T. J. Martínez, "Direct QM/MM excited-state dynamics of retinal protonated Schiff base in isolation and methanol solution," J. Phys. Chem. B **119**, 704–714 (2015).
[6] M. Ruckenbauer, M. Barbatti, T. Müller, and H. Lischka, "Nonadiabatic photodynamics of a retinal model in polar and nonpolar environment," J. Phys. Chem. A **117**, 2790–2799 (2013).
[7] E. Pieri, A. R. Walker, M. Zhu, and T. J. Martínez, "Conical intersection accessibility dictates brightness in red fluorescent proteins," J. Am. Chem. Soc. **146**, 17646–17658 (2024).
[8] G. A. Worth, H.-D. Meyer, H. Köppel, L. S. Cederbaum, and I. Burghardt, "Using the MCTDH wavepacket propagation method to describe multimode non-adiabatic dynamics," Int. Rev. Phys. Chem. **27**, 569–606 (2008).
[9] A. Kühl and W. Domcke, "Multilevel Redfield description of the dissipative dynamics at conical intersections," J. Chem. Phys. **116**, 263–274 (2002).
[10] A. Raab, I. Burghardt, and H.-D. Meyer, "The multiconfiguration time-dependent Hartree method generalized to the propagation of density operators," J. Chem. Phys. **111**, 8759–8772 (1999).

[11] A. Kelly and R. Kapral, "Quantum-classical description of environmental effects on electronic dynamics at conical intersections," J. Chem. Phys. **133**, 084502 (2010).
[12] M. H. Beck, A. Jäckle, G. A. Worth, and H. D. Meyer, "The multiconfiguration time-dependent Hartree (MCTDH) method: A highly efficient algorithm for propagating wavepackets," Phys. Rep. **324**, 1–105 (2000).
[13] H. Wang, "Multilayer multiconfiguration time-dependent Hartree theory," J. Phys. Chem. A **119**, 7951–7965 (2015).
[14] H. Wang and M. Thoss, "Multilayer formulation of the multiconfiguration time-dependent Hartree theory," J. Chem. Phys. **119**, 1289–1299 (2003).
[15] O. Vendrell and H.-D. Meyer, "Multilayer multiconfiguration time-dependent Hartree method: Implementation and applications to a Henon–Heiles Hamiltonian and to pyrazine," J. Chem. Phys. **134**, 044135 (2011).
[16] U. Manthe, "A multilayer multiconfigurational time-dependent Hartree approach for quantum dynamics on general potential energy surfaces," J. Chem. Phys. **128**, 164116 (2008).
[17] U. Schollwöck, "The density-matrix renormalization group in the age of matrix product states," Ann. Phys. **326**, 96–192 (2011).
[18] S. R. White and A. E. Feiguin, "Real-time evolution using the density matrix renormalization group," Phys. Rev. Lett. **93**, 076401 (2004).
[19] T. Lenzen and U. Manthe, "Neural network based coupled diabatic potential energy surfaces for reactive scattering," J. Chem. Phys. **147**, 084105 (2017).
[20] W. Koch and D. H. Zhang, "Communication: Separable potential energy surfaces from multiplicative artificial neural networks," J. Chem. Phys. **141**, 021101 (2014).
[21] D. M. G. Williams and W. Eisfeld, "Complete nuclear permutation inversion invariant artificial neural network (CNPI-ANN) diabatization for the accurate treatment of vibronic coupling problems," J. Phys. Chem. A **124**, 7608–7621 (2020).
[22] G. W. Richings and S. Habershon, "MCTDH on-the-fly: Efficient grid-based quantum dynamics without pre-computed potential energy surfaces," J. Chem. Phys. **148**, 134116 (2018).
[23] I. Polyak, G. W. Richings, S. Habershon, and P. J. Knowles, "Direct quantum dynamics using variational Gaussian wavepackets and Gaussian process regression," J. Chem. Phys. **150**, 041101 (2019).
[24] Y. Shu and D. G. Truhlar, "Diabatization by machine intelligence," J. Chem. Theory Comput. **16**, 6456–6464 (2020).
[25] Y. M. Thant, T. Wakamiya, M. Nukunudompanich, K. Kameda, M. Ihara, and S. Manzhos, "Kernel regression methods for prediction of materials properties: Recent developments," Chem. Phys. Rev. **6**, 011306 (2025).
[26] W. Koch, M. Bonfanti, P. Eisenbrandt, A. Nandi, B. Fu, J. Bowman, D. Tannor, and I. Burghardt, "Two-layer Gaussian-based MCTDH study of the $S_1 \leftarrow S_0$ vibronic absorption spectrum of formaldehyde using multiplicative neural network potentials," J. Chem. Phys. **151**, 064121 (2019).
[27] B. Błasiak, D. Brey, W. Koch, R. Martinazzo, and I. Burghardt, "Modelling ultrafast dynamics at a conical intersection with regularized diabatic states: An approach based on multiplicative neural networks," Chem. Phys. **560**, 111542 (2022).
[28] B. Błasiak, D. Brey, R. Martinazzo, and I. Burghardt, "Quantum dynamics at a conical intersection in solution. I. Multiplicative neural networks and thermofields," J. Chem. Phys. **163**, 124108 (2025).
[29] S. Mukamel, *Principles of Nonlinear Optical Spectroscopy* (Oxford University Press, 1995).
[30] A. Nitzan, *Chemical Dynamics in Condensed Phases: Relaxation, Transfer, and Reactions in Condensed Molecular Systems* (Oxford University Press, 2014).
[31] V. May and O. Kühn, *Charge and Energy Transfer Dynamics in Molecular Systems*, 3rd ed. (Wiley VCH, 2011).
[32] L. S. Cederbaum, E. Gindensperger, and I. Burghardt, "Short-time dynamics through conical intersections in macrosystems," Phys. Rev. Lett. **94**, 113003 (2005).
[33] E. Gindensperger, I. Burghardt, and L. S. Cederbaum, "Short-time dynamics through conical intersections in macrosystems. II. Applications," J. Chem. Phys. **124**, 144104 (2006).
[34] I. Burghardt, E. Gindensperger, and L. S. Cederbaum, "An effective Hamiltonian for the short-time dynamics at a conical intersection," Mol. Phys. **104**, 1081–1093 (2006).
[35] I. Burghardt, K. H. Hughes, R. Martinazzo, H. Tamura, E. Gindensperger, H. Köppel, and L. S. Cederbaum, "Conical intersections coupled to an environment," in *Conical Intersections*, edited by W. Domcke, D. R. Yarkony, and H. Köppel (World Scientific, 2011), pp. 301–346.
[36] I. Burghardt, L. S. Cederbaum, and J. T. Hynes, "Environmental effects on a conical intersection: A model study," Faraday Discuss. **127**, 395 (2004).
[37] I. Burghardt and J. T. Hynes, "Excited-state charge transfer at a conical intersection: Effects of an environment," J. Phys. Chem. A **110**, 11411–11423 (2006).
[38] C.-P. Hsu, "Reorganization energies and spectral densities for electron transfer problems in charge transport materials," Phys. Chem. Chem. Phys. **22**, 21630–21641 (2020).
[39] V. Butkus, L. Valkunas, and D. Abramavicius, "Molecular vibrations-induced quantum beats in two-dimensional electronic spectroscopy," J. Chem. Phys. **137**, 044513 (2012).
[40] G. Zgrablić, A. M. Novello, and F. Parmigiani, "Population branching in the conical intersection of the retinal chromophore revealed by multipulse ultrafast optical spectroscopy," J. Am. Chem. Soc. **134**, 955–961 (2012).
[41] G. Bassolino, T. Sovdat, M. Liebel, C. Schnedermann, B. Odell, T. D. W. Claridge, P. Kukura, and S. P. Fletcher, "Synthetic control of retinal photochemistry and photophysics in solution," J. Am. Chem. Soc. **136**, 2650–2658 (2014).
[42] G. Bassolino, T. Sovdat, A. Soares Duarte, J. M. Lim, C. Schnedermann, M. Liebel, B. Odell, T. D. W. Claridge, S. P. Fletcher, and P. Kukura, "Barrierless photoisomerization of 11-cis retinal protonated Schiff base in solution," J. Am. Chem. Soc. **137**, 12434–12437 (2015).
[43] H. V. Kiefer, E. Gruber, J. Langeland, P. A. Kusochek, A. V. Bochenkova, and L. H. Andersen, "Intrinsic photoisomerization dynamics of protonated Schiff-base retinal," Nat. Commun. **10**, 1210 (2019).
[44] J. N. Bull, C. W. West, C. S. Anstöter, G. da Silva, E. J. Bieske, and J. R. R. Verlet, "Ultrafast photoisomerisation of an isolated retinoid," Phys. Chem. Chem. Phys. **21**, 10567–10579 (2019).
[45] I. Burghardt, L. S. Cederbaum, and J. T. Hynes, "Ultrafast excited-state charge transfer at a conical intersection: Effects of an environment," Comput. Phys. Commun. **169**, 95–98 (2005), part of Special Issue: Proceedings of the Europhysics Conference on Computational Physics 2004.
[46] J. P. Malhado and J. T. Hynes, "Photoisomerization for a model protonated Schiff base in solution: Sloped/peaked conical intersection perspective," J. Chem. Phys. **137**, 22A543 (2012).
[47] J. P. Malhado, R. Spezia, and J. T. Hynes, "Dynamical friction effects on the photoisomerization of a model protonated Schiff base in solution," J. Phys. Chem. A **115**, 3720–3735 (2011).
[48] Y. Takahashi and H. Umezawa, "Thermo field dynamics," Int. J. Mod. Phys. B **10**, 1755–1805 (1996).
[49] S. M. Barnett and P. L. Knight, "Thermofield analysis of squeezing and statistical mixtures in quantum optics," J. Opt. Soc. Am. B **2**, 467 (1985).
[50] R. Borrelli and M. F. Gelin, "Finite temperature quantum dynamics of complex systems: Integrating thermo-field theories and tensor-train methods," Wiley Interdiscip. Rev.: Comput. Mol. Sci. **11**, e1539 (2021).
[51] A. Garg, J. N. Onuchic, and V. Ambegaokar, "Effect of friction on electron transfer in biomolecules," J. Chem. Phys. **83**, 4491–4503 (1985).
[52] H. Köppel, J. Gronki, and S. Mahapatra, "Construction scheme for regularized diabatic states," J. Chem. Phys. **115**, 2377–2388 (2001).
[53] H. Köppel, "Regularized diabatic states and quantum dynamics on intersecting potential energy surfaces," Faraday Discuss. **127**, 35–47 (2004).
[54] M. F. Gelin and R. Borrelli, "Thermal Schrödinger equation: Efficient tool for simulation of many-body quantum dynamics at finite temperature," Ann. Phys. **529**, 1700200 (2017).
[55] B. Błasiak, D. Brey, R. Martinazzo, and I. Burghardt, "Reduced density matrices and phase-space distributions in thermofield dynamics," arXiv:2505.21302 [quant-ph] (2025).
[56] G. A. Worth, M. H. Beck, A. Jäckle, and H. Meyer, The MCTDH package, 2015; see http://www.pci.uni-heidelberg.de/tc/usr/mctdh/.
[57] U. Weiss, *Quantum Dissipative Systems* (World Scientific, 2012).

[58]K. H. Hughes, C. D. Christ, and I. Burghardt, "Effective-mode representation of non-Markovian dynamics: A hierarchical approximation of the spectral density. I. Application to single surface dynamics," J. Chem. Phys. **131**, 024109 (2009).
[59]K. H. Hughes, C. D. Christ, and I. Burghardt, "Effective-mode representation of non-Markovian dynamics: A hierarchical approximation of the spectral density. II. Application to environment-induced nonadiabatic dynamics," J. Chem. Phys. **131**, 124108 (2009).
[60]R. Martinazzo, B. Vacchini, K. H. Hughes, and I. Burghardt, "Communication: Universal Markovian reduction of Brownian particle dynamics," J. Chem. Phys. **134**, 011101 (2011).
[61]R. Martinazzo, K. H. Hughes, and I. Burghardt, "Unraveling a Brownian particle's memory with effective mode chains," Phys. Rev. E **84**, 030102(R) (2011).
[62]W. Popp, M. Polkehn, K. H. Hughes, R. Martinazzo, and I. Burghardt, "Vibronic coupling models for donor-acceptor aggregates using an effective-mode scheme: Application to mixed Frenkel and charge-transfer excitons in oligothiophene aggregates," J. Chem. Phys. **150**, 244114 (2019).
[63]I. de Vega and M.-C. Bañuls, "Thermofield-based chain-mapping approach for open quantum systems," Phys. Rev. A **92**, 052116 (2015).
[64]D. Tamascelli, A. Smirne, J. Lim, S. Huelga, and M. Plenio, "Efficient simulation of finite-temperature open quantum systems," Phys. Rev. Lett. **123**, 090402 (2019).
[65]H. Takahashi and R. Borrelli, "Effective modeling of open quantum systems by low-rank discretization of structured environments," J. Chem. Phys. **161**, 151101 (2024).
[66]H. Takahashi and R. Borrelli, "Discretization of structured bosonic environments at finite temperature by interpolative decomposition: Theory and application," J. Chem. Theory Comput. **21**, 2206–2218 (2025).
[67]L. Wang, L. Chen, N. Zhou, and Y. Zhao, "Variational dynamics of the sub-Ohmic spin-boson model on the basis of multiple Davydov D_1 states," J. Chem. Phys. **144**, 024101 (2016).
[68]H. Takahashi, S. Rudge, C. Kaspar, M. Thoss, and R. Borrelli, "High accuracy exponential decomposition of bath correlation functions for arbitrary and structured spectral densities: Emerging methodologies and new approaches," J. Chem. Phys. **160**, 204105 (2024).
[69]I. de Vega, U. Schollwöck, and F. A. Wolf, "How to discretize a quantum bath for real-time evolution," Phys. Rev. B **92**, 155126 (2015).
[70]W. P. Schleich, *Quantum Optics in Phase Space*, 1st ed. (Wiley-VCH Verlag Berlin GmbH, 2001).
[71]S. Gozem, P. J. M. Johnson, A. Halpin, H. L. Luk, T. Morizumi, V. I. Prokhorenko, O. P. Ernst, M. Olivucci, and R. J. D. Miller, "Excited-state vibronic dynamics of bacteriorhodopsin from two-dimensional electronic photon echo spectroscopy and multiconfigurational quantum chemistry," J. Phys. Chem. Lett. **11**, 3889–3896 (2020).
[72]K. Herasymenko, D. Walisinghe, M. Konno, L. Barneschi, I. de Waele, M. Sliwa, K. Inoue, M. Olivucci, and S. Haacke, "Archaerhodopsin 3 is an ideal template for the engineering of highly fluorescent optogenetic reporters," Chem. Sci. **16**, 761–774 (2025).
[73]I. C. D. Merritt, D. Jacquemin, and M. Vacher, "Nonadiabatic coupling in trajectory surface hopping: How approximations impact excited-state reaction dynamics," J. Chem. Theory Comput. **19**, 1827–1842 (2023).
[74]G. J. Atchity, S. S. Xantheas, and K. Ruedenberg, "Potential energy surfaces near intersections," J. Chem. Phys. **95**, 1862–1876 (1991).
[75]W. Popp, D. Brey, R. Binder, and I. Burghardt, "Quantum dynamics of exciton transport and dissociation in multichromophoric systems," Annu. Rev. Phys. Chem. **72**, 591–616 (2021).
[76]H. Chen, B. Roux, and C. Chipot, "Discovering reaction pathways, slow variables, and committor probabilities with machine learning," J. Chem. Theory Comput. **19**, 4414–4426 (2023).